

**Stefan Riedel
and Franz Zotter**

Institute of Electronic Music and Acoustics
University of Music and Performing Arts
Inffeldgasse 10/3, 8010 Graz, Austria
{riedel, zotter}@iem.at

Design, Control, and Evaluation of Mixed-Order, Compact Spherical Loudspeaker Arrays

Abstract: Beamforming on the icosahedral loudspeaker (IKO), a compact, spherical loudspeaker array, was recently established and investigated as an instrument to produce auditory sculptures (i.e., 3-D sonic imagery) in electroacoustic music. Sound beams in the horizontal plane most effectively and expressively produce auditory objects via lateral reflections on sufficiently close walls and baffles. Can there be 3-D-printable arrays at drastically reduced cost and transducer count, but with similarly strong directivity in the horizontal plane? To find out, we adopt mixed-order Ambisonics schemes to control fewer, and predominantly horizontal, beam patterns, and we propose the 3|9|3 array as a suitable design, with beamforming crossing over to Ambisonics panning at high frequencies. Analytic models and measurements on hardware prototypes permit a comparison between the new design and the IKO regarding beamforming capacity. Moreover, we evaluate our 15-channel 3|9|3 prototype in listening experiments to find out whether the sculptural qualities and auditory object trajectories it produces are comparable to those of the 20-channel IKO.

Early work on compact, spherical loudspeaker arrays with controllable directivity was described by Warusfel, Derogis, and Causse (1997) and by Pollow and Behler (2009). Platonic solids (regular convex polyhedra, such as dodecahedra or icosahedra) offer practical housings because of their symmetries and their small number of faces, each of which can contain a loudspeaker pointing outward in a unique direction. Conventional spherical beamforming on the 12 transducers of a dodecahedron uses spherical harmonics up to the second order, while on the 20 transducers of the icosahedron, it is limited to third order. To overcome the limitation, array-specific acoustic radiation modes have been proposed by Pasqual et al. (2010), but those modes would require a frequency-dependent beam encoding. Alternatively, the number of transducers per surface has been increased beyond one, e.g., to six per each of the 20 icosahedral facets by Avizienis et al. (2006), which, however, is only practical with high-frequency tweeters because of their small size.

Recently, Zotter et al. (2017) presented the icosahedral loudspeaker (IKO) as an instrument for electroacoustic music in an article in this journal that outlines the theoretical principles of spherical

beamforming and exemplary practical tools required for its use (ambix and mcfx VST plugins). Wendt et al. (2017b) and Sharma, Frank, and Zotter (2019) investigated auditory sculptures and their attributes that emerge for exemplary static and time-varying beam compositions, and hereby provide a descriptive framework for the artistic practice. In these beam compositions, sound is projected onto walls and baffles to produce auditory objects via acoustic reflections, essentially via horizontal beams, that are most effective. This article investigates an alternative, 3-D-printable, compact spherical loudspeaker array design customized to producing horizontal beams.

Figure 1 shows the IKO and the proposed compact spherical loudspeaker array design that features a horizontal ring of transducers but also supplementary ones above and below. A single horizontal ring might appear sufficient, but the directional definition of the resulting beam shape can be of poor vertical resolution. For compact spherical microphone arrays, Márton Marschall (2014) describes mixed-order schemes that effectively reduce the number of transducers by neglecting certain vertical spherical harmonic modes to maintain a high horizontal resolution. As the gap between horizontal and overall resolution cannot be overly stretched for robust beamforming, Chang and Marschall (2018) present alternative lattice schemes. We present here the use of a mixed-order scheme to efficiently increase the horizontal resolution of compact,

Computer Music Journal, 44:4, pp. 60–76, Winter 2020
doi:10.1162/COMJ_a_00581

© 2021 Massachusetts Institute of Technology. Published under a Creative Commons Attribution 4.0 International (CC BY 4.0) license.

Figure 1. The icosahedral array (IKO) on the left and the 3|9|3 array on the right are typically staged in front of reflective baffles. As a nomenclature we

define $n_e|n_h|n_e$ to refer to a layout with n_h transducers in the horizontal ring, and n_e transducers in the upper and lower ring (at non-zero elevation).

Figure 2. Spherical harmonics control scheme for the 3|9|3 array (a), and the corresponding mixed-order directivity

pattern (b), where the black line indicates a horizontal cut and the gray line indicates a vertical cut.

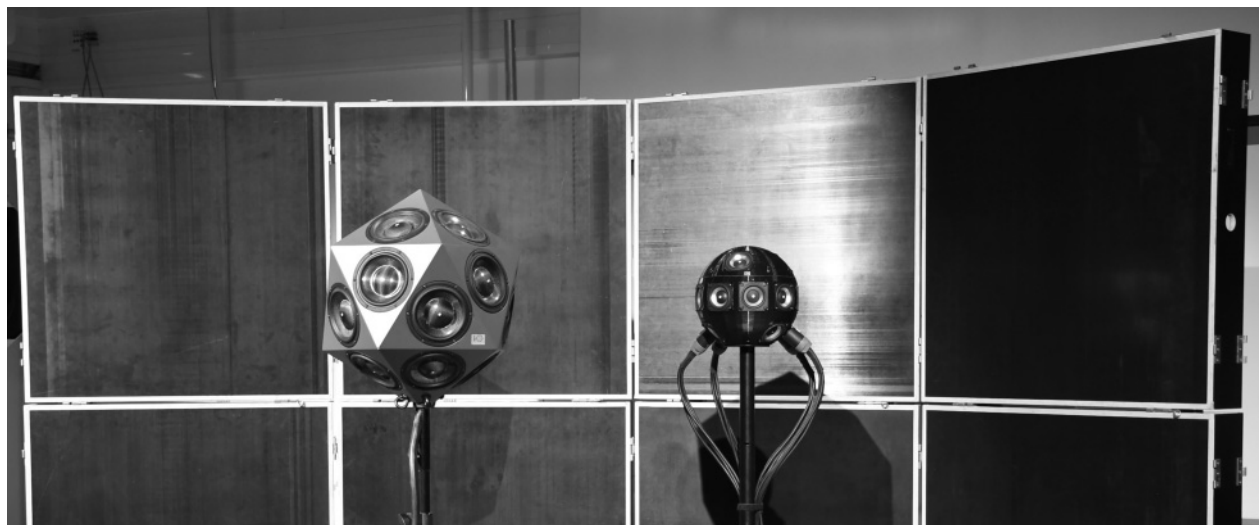


Figure 1.

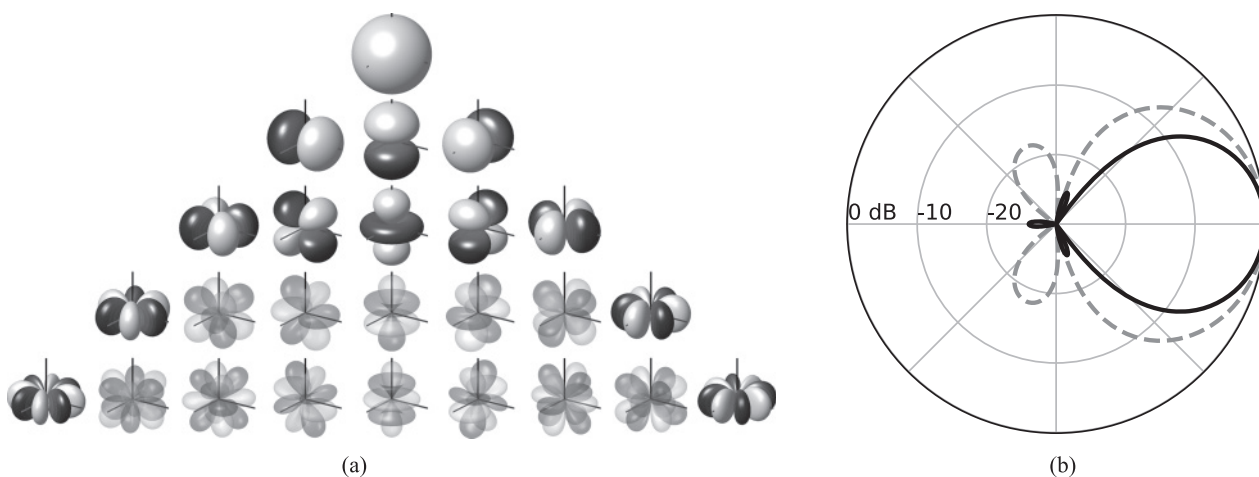


Figure 2.

spherical loudspeaker arrays. Figure 2a shows the spherical harmonics as basis patterns that are superimposed in spherical beamforming to create narrow sound beams with variable direction. The concept is the same as in Ambisonics, however, radiating outwards from the compact array. A fourth-order horizontal and second-order vertical mixed-order control omits some of the spherical harmonics (translucent in Figure 2), and hereby

produces a beam pattern that is more focused horizontally than vertically (cf. Figure 2b).

The article begins with a presentation of the proposed mixed-order schemes to increase the horizontal resolution of, for example, dodecahedral arrays from second to third order and icosahedral arrays from third to fourth order. Its main targets are new three-ring layouts and their scheme to effectively reduce the number of transducers.

The Array Simulation section numerically simulates the mixed-order layouts and compares their beamforming capacity based on 2-D and 3-D metrics of effective beamforming order. Modal beamforming on common-enclosure loudspeaker arrays requires decoupling of the transducer movements and radial filtering, which is not productive at high frequencies. The Control Filter Design section introduces a measurement-based, low-latency, two-band process with regularization at low frequencies to minimize filter lengths and All-Round Ambisonics Decoding (AllRAD) panning at high frequencies for minimal grating lobes. The Directivity Measurements section verifies the gain in beamforming capacity of the new processing scheme and the 3|9|3 loudspeaker, as depicted in Figure 1, based on openly accessible measurement data. The final Listening Experiments section assesses auditory sculpture attributes and auditory trajectories obtained with the 3|9|3 loudspeaker, comparing them to those of the IKO.

Normalized Mixed-Order Directivity Patterns

Directivity functions for spherical beamforming or Ambisonics panning use a finite-order (i.e., resolution-limited) representation of a Dirac delta $\delta(\theta_{\text{beam}}^T \theta - 1)$ directed towards θ_{beam} and evaluated in the variable direction θ ,

$$g(\theta) = \sum_{n=0}^N \sum_{m=-n}^n w_{nm} Y_n^m(\theta) Y_n^m(\theta_{\text{beam}}), \quad (1)$$

where both of the direction unit vectors θ and θ_{beam} are Cartesian unit vectors $\theta = [\cos \varphi \sin \vartheta, \sin \varphi \sin \vartheta, \cos \vartheta]^T$ depending on the azimuth angle φ and zenith angle ϑ ; or φ_{beam} and ϑ_{beam} in case of θ_{beam} . Y_n^m are the spherical harmonics, and typically, to avoid side lobes, the weights $w_{nm} = w_n$ are the max- r_E weights approximated by Zotter and Frank (2012):

$$w_n = P_n \left[\cos \left(\frac{\pi}{180} \frac{137.9}{N+1.51} \right) \right], \quad (2)$$

where P_n are the Legendre polynomials.

Defining the vectors

$$\begin{aligned} \mathbf{y}_N(\theta) &= [Y_n^m(\theta)]_{n=0\dots N, m=-n\dots n}, \\ \mathbf{w}_N &= [w_n]_{n=0\dots N, m=-n\dots n}, \end{aligned} \quad (3)$$

Equation 1 can be rewritten as

$$g(\theta) = \mathbf{y}_N(\theta)^T \text{diag}\{\mathbf{w}_N\} \mathbf{y}_N(\theta_{\text{beam}}), \quad (4)$$

which defines a rotationally symmetric directivity pattern. The directivity function of mixed order differs from this by a mask \mathbf{M} that selects a subset of fewer spherical harmonics; see Figures 2 and 3. The mask \mathbf{M} has $(N+1)^2$ columns, each representing a spherical harmonic, and fewer rows, of which each selects one of the harmonics to be a mixed-order component:

$$\begin{aligned} g_M(\theta) &= \mathbf{y}_N(\theta)^T \mathbf{M}^T \text{diag}\{\tilde{\mathbf{w}}_M\} \mathbf{M} \mathbf{y}_N(\theta_{\text{beam}}) \\ &= \mathbf{y}_M(\theta)^T \text{diag}\{\tilde{\mathbf{w}}_M\} \mathbf{y}_M(\theta_{\text{beam}}). \end{aligned} \quad (5)$$

The redefined weights $\tilde{\mathbf{w}}_M$ restore the balance of the horizontal circular-harmonic content that is represented by fewer max- r_E -weighted components in every degree m for mixed order. To get $\tilde{\mathbf{w}}_M = [\tilde{w}_{nm}^{(M)}]$ we choose the unit vector $\mathbf{u}_x = [1, 0, 0]^T$ to the x direction

$$\tilde{w}_{nm}^{(M)} = w_n \frac{\sum_{n'=|m|}^N [Y_{n'}^{|m|}(\mathbf{u}_x)]^2 w_{n'}}{\sum_{n'=|m|}^N [Y_{n'}^{|m|}(\mathbf{u}_x)]^2 w_{n'} M_{n'|m|}}. \quad (6)$$

Mixed-Order Transducer Layouts

The mixed-order schemes in Figure 3 and the associated spherical harmonic subsets can be controlled using either Platonic layouts or the new three-ring layouts consisting of an upper, a horizontal, and a lower ring. The nomenclature $n_e|n_h|n_e$ refers to a specific layout, for example, the 3|9|3 layout with $n_h = 9$ transducers in the horizontal ring and $n_e = 3$ transducers in the two other rings. The Platonic arrays can also be seen as three-ring layouts, with the middle ring being a zigzag ring of loudspeakers

Figure 3. Control schemes for the third-order dodecahedron (a), fourth-order IKO (b), and the new mixed-order layouts 1|7|1 (c), 3|9|3 (d), 4|8|4 (e), and 5|10|5 (f). Rows indicate the

spherical harmonics order $n = 0 \dots 4$ and columns indicate the degrees $m = -n \dots n$. Gray squares indicate controlled spherical harmonics, white squares indicate uncontrolled ones. The

third-order dodecahedral scheme (a) also holds for the 3|7|3 layout. For brevity, the second-order dodecahedral and third-order icosahedral schemes are not shown.

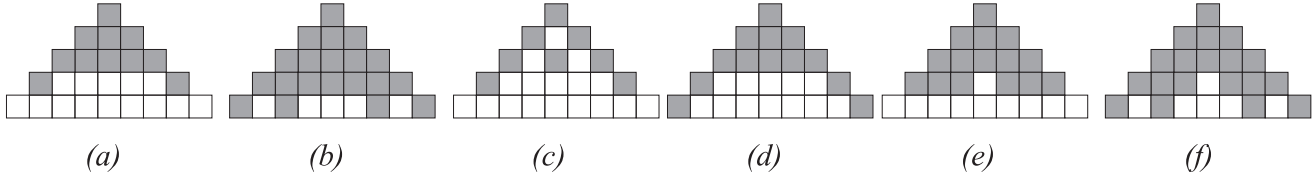


Table 1. Coordinates of Mixed-Order Layouts

	5 10 5	4 8 4	3 9 3	3 7 3
φ , at $\vartheta = 90^\circ$	0:36:324	0:45:315	20:40:340	0:51.4:308.6
φ , at $\vartheta = 45^\circ$	18:72:306	0:90:270	0:120:240	20:120:26
φ , at $\vartheta = 135^\circ$	54:72:342	45:90:315	60:120:300	80:120:320

Coordinates are denoted as [start:step:stop] degrees of azimuthal coordinates of the horizontal, upper, and lower ring of a layout. Zenith coordinates are $\vartheta = [90^\circ, 45^\circ, 135^\circ]$ for horizontal, upper, and lower ring respectively. The 1|7|1-layout (not shown) is an exception: The nonhorizontal positions are the poles $\vartheta = [0^\circ, 180^\circ]$.

oriented at positive and negative elevation angles in alternation. That is, the dodecahedron as a 1|10|1 layout and the icosahedron as a 5|10|5 layout, which yields extended mixed-order control schemes for those Platonic arrays. The coordinates of the new three-ring layouts are given in Table 1.

According to Jérôme Daniel (2001), the number of transducers n_h in the horizontal ring determines the maximum achievable 2-D order N_{2D} ,

$$n_h \geq 2 N_{2D} + 1. \quad (7)$$

The n_e transducers in the upper and lower rings are added to stabilize beamforming vertically.

We regard the condition number κ of the mixed-order spherical harmonics matrix \mathbf{Y}_M evaluated at the transducer coordinates θ_l , to ensure a well-conditioned pseudoinverse that is required to control the array,

$$\mathbf{Y}_M = \mathbf{M} \mathbf{Y}_N, \quad (8)$$

with $\mathbf{Y}_N = [Y_n^m(\theta_l)]_{n=0 \dots N, m=-n \dots n}^{l=1 \dots L}$.

Table 2 shows that all \mathbf{Y}_M matrices (subsets see Figure 3) are sufficiently well-conditioned as $\kappa(\mathbf{Y}_M)$ is finite and close to unity.

Table 2. Transducer Counts and Condition Numbers

	L	κ
Dodecahedron	12	1.6
Icosahedron	20	2.4
1 7 1	9	1.6
3 7 3	13	2.0
3 9 3	15	1.9
4 8 4	16	1.7
5 10 5	20	1.8

Number of transducers L and the condition number κ of \mathbf{Y}_M used in the speaker configurations.

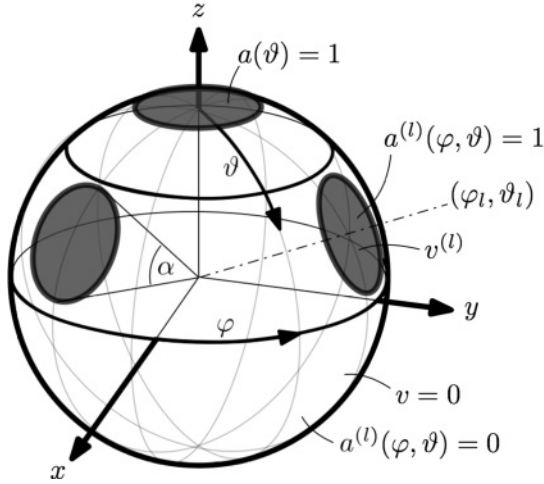
Array Simulation

In the following we numerically simulate the mixed-order layouts by means of the spherical cap model and compare their beamforming capacity based on 2-D and 3-D metrics of effective beamforming order.

Spherical Cap Model for Sound Radiation

To acoustically simulate the beamforming performance of various array layouts, a reasonably

Figure 4. Spherical-cap model: $a^{(l)}(\varphi, \vartheta)$ denotes the aperture function of the l^{th} loudspeaker cap, $v^{(l)}$ the l^{th} cap velocity.



high-order model, with $\hat{N} = 35$, was applied by Zotter and Höldrich (2007), assuming moving spherical caps at the loudspeaker positions on an otherwise rigid sphere, see Figure 4. Cap-shaped surface velocity distributions can be expressed in the spherical harmonics domain as coefficients $v_{nm}(R)$ at a radius R that can be extrapolated to a far-field sound pressure at the frequency ω in radians (Zotter and Frank 2019, ch. 7.3):

$$p(\boldsymbol{\theta}) = \sum_{n=0}^{\hat{N}} \frac{i^n}{k h'_n(kR)} \sum_{m=-n}^n v_{nm}|_R Y_n^m(\boldsymbol{\theta}), \quad (9)$$

with real-valued spherical harmonics Y_n^m , and the frequency dependency via the derivative h'_n of the spherical Hankel function of the second kind h_n , evaluated at the wave number $k = \omega/c$ times array radius R , with the frequency $\omega = 2\pi f$ in radians per second and the imaginary unit i . In our case, the velocity coefficient v_{nm} is computed as a sum over the L cap apertures $a_{nm}^{(l)}$ weighted by the velocities $v^{(l)}$

$$v_{nm}|_R = \sum_{l=1}^L a_{nm}^{(l)} v^{(l)}. \quad (10)$$

The coefficients of the cap a_{nm}^l around the l -th transducer's direction $\boldsymbol{\theta}_l$ are obtained by spherical convolution of a polar cap a_n of the aperture α around $z = 1$ using

$$a_{nm}^{(l)} = a_n Y_n^m(\boldsymbol{\theta}_l), \quad (11)$$

with $a_n = 2\pi \int_{\cos(\alpha/2)}^1 P_n(z) dz$,

where

P_n is the Legendre polynomial
(see Zotter and Frank 2019),

$$a_0 = 2\pi(1 - \cos \frac{\alpha}{2}), \text{ and}$$

$$a_n = 2\pi \frac{\cos \frac{\alpha}{2} P_n(\cos \frac{\alpha}{2}) - P_{n+1}(\cos \frac{\alpha}{2})}{n} \text{ for } n > 0.$$

The model can be written in matrix form

$$p(\boldsymbol{\theta}) = \mathbf{y}(\boldsymbol{\theta})^T \text{diag}\{\mathbf{h}(\omega)\} \text{diag}\{\mathbf{a}\} \mathbf{Y} \mathbf{v}. \quad (12)$$

The matrices and vectors used are defined as

$$\begin{aligned} \mathbf{h}(\omega) &= \left[\frac{i^n}{k h'_n(kR)} \right]_{n=0, \dots, \hat{N}, m=-n, \dots, n} \\ \mathbf{a} &= [a_n]_{n=0, \dots, \hat{N}, m=-n, \dots, n} \\ \mathbf{y}(\boldsymbol{\theta}) &= [Y_n^m(\boldsymbol{\theta})]_{n=0, \dots, \hat{N}, m=-n, \dots, n} \\ \mathbf{Y} &= [\mathbf{y}(\boldsymbol{\theta}_1) \dots \mathbf{y}(\boldsymbol{\theta}_L)]. \end{aligned} \quad (13)$$

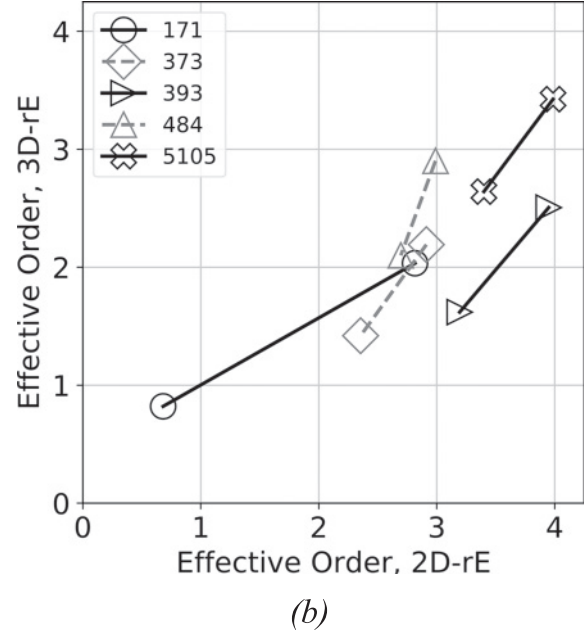
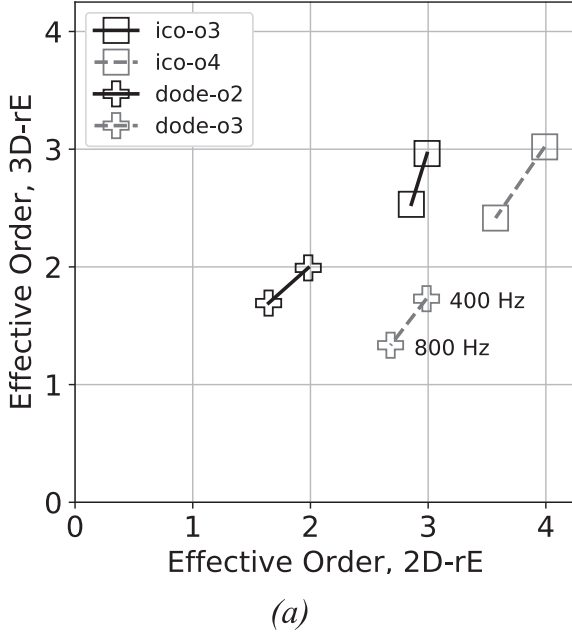
Modal beamforming yields the cap velocities \mathbf{v} in Equation 12 for a desired beam pattern in the controllable mixed-order subspace. It is described by running the weighted beam steering $\text{diag}\{\tilde{\mathbf{w}}_M\} \mathbf{y}_M(\boldsymbol{\theta}_{\text{beam}})$ through the inverse propagator and aperture, and pseudoinverse rectangular matrix \mathbf{Y}_M^+ of the cap positions, all in the mixed-order subspace

$$\begin{aligned} \mathbf{v} &= \mathbf{Y}_M^+ \text{diag}\{\mathbf{a}_M\}^{-1} \text{diag}\{\mathbf{h}_M(\omega)\}^{-1} \text{diag}\{\tilde{\mathbf{w}}_M\} \\ &\quad \mathbf{y}_M(\boldsymbol{\theta}_{\text{beam}}). \end{aligned} \quad (14)$$

Figure 5. The 2-D and 3-D effective orders of a simulated horizontal beam. Two markers per layout indicate results at 400 Hz in the operation range $kR < N$ and 800 Hz

where spatial aliasing becomes noticeable $kR \approx N$; with $N = 3$ and radius $R = 0.21$ m. Platonic arrays gain a full order (in 2-D) with mixed-order control (a).

The 3|9|3-array achieves fourth order in the 2-D rating with five transducers fewer than the IKO (b). Longer lines indicate poor robustness against spatial aliasing.



Simulation Results

The results of the simulations are analyzed over frequency by means of a scalar measure of the beam focus. For the analysis of the focus in three dimensions, the simulated beam pattern was spherically sampled by the set of directions $\{\theta_j\}$ of a $J = 5,100$ -point t-design (Chebyshev-type quadrature; cf. Gräf 2013) to compute the energy vector \mathbf{r}_E measure

$$\mathbf{r}_E^{(3D)} = \frac{\sum_{j=1}^J |p(\theta_j)|^2 \theta_j}{\sum_{j=1}^J |p(\theta_j)|^2}. \quad (15)$$

To exclusively evaluate the beam focus in the horizontal plane, equiangular sampling of the azimuth was used ($J = 72$, i.e., 5° steps, $\phi_j = 2\pi(j-1)/J$) with the measure

$$\mathbf{r}_E^{(2D)} = \frac{\sum_{j=1}^J |p(\phi_j + \varphi_{\text{beam}})|^2 |\sin \phi_j| \begin{pmatrix} \cos \phi_j \\ \sin \phi_j \end{pmatrix}}{\sum_{j=1}^J |p(\phi_j + \varphi_{\text{beam}})|^2 |\sin \phi_j|}. \quad (16)$$

It involves surface weights $|\sin \phi_j|$ representing the share of each sample of a spherical surface. The

weights imply the optimistic interpretation of the 2-D pattern $p(\phi_j + \varphi_{\text{beam}})$ centered at the beam-forming azimuth φ_{beam} as rotationally symmetric in 3-D. The 2-D and 3-D measures hereby match, $\|\mathbf{r}_E^{(2D)}\| = \|\mathbf{r}_E^{(3D)}\|$, whenever a measured pattern is more or less isotropic, and there is a mismatch $\|\mathbf{r}_E^{(2D)}\| > \|\mathbf{r}_E^{(3D)}\|$ whenever the horizontal focus is stronger than the global one, as targeted by the proposed mixed-order designs.

The effective order $N_{\text{eff},3D}$ of the 3-D pattern or the effective order $N_{\text{eff},2D}$ of its 2-D horizontal cut is evaluated as inverse of the order-dependent maximum $\max \|\mathbf{r}_E\| = \cos((\pi/180)(137.9/(N + 1.51)))$,

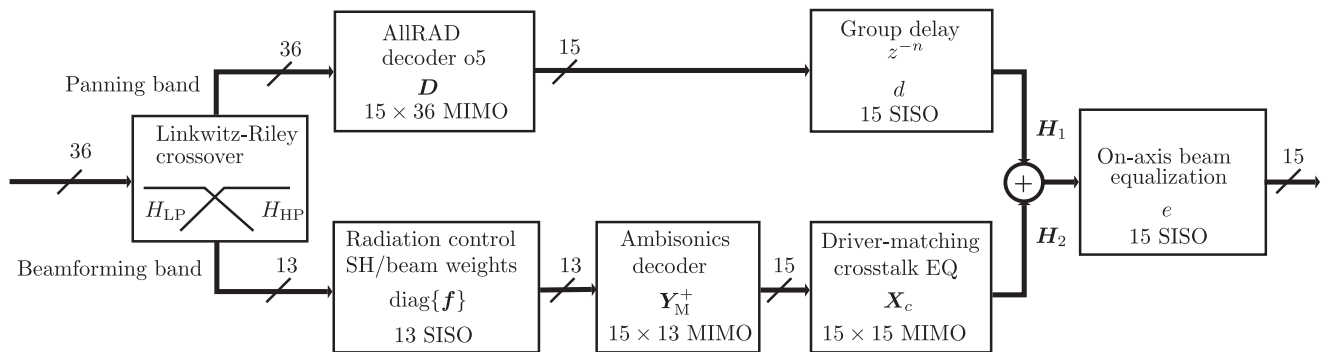
$$N_{\text{eff}} = \frac{\pi}{180} \frac{137.9}{\arccos \|\mathbf{r}_E\|} - 1.51, \quad (17)$$

from the respective $\mathbf{r}_E^{(3D)}$ or $\mathbf{r}_E^{(2D)}$ values estimated by Equations 15 or 16.

The simulation results for a cap aperture angle $\alpha = 36^\circ$ and a radius $R = 0.21$ m in Figure 5a indicate improvement of the 2-D focus with Platonic arrays (dodecahedral and icosahedral) by one order when

Figure 6. Control block diagram, for the example of a 3|9|3-array with $L = 15$, $(N + 1)^2 = 36$ and 13 controlled harmonics

(MIMO: multiple-input, multiple-output; SISO: single-input, single-output).



using the proposed mixed-order control, at some loss in the 3-D focus metric for the dodecahedral array. As seen in Figure 5b, the specific mixed-order layouts 4|8|4 and 3|9|3, respectively, reach or exceed the 2-D beam focus of the icosahedral layout, but with four to five fewer transducers, validating the mixed-order concept for compact loudspeaker arrays.

An OpenSCAD model of the 3|9|3 array was created to 3-D-print the necessary spherical housing (open access at https://git.iem.at/s1330219/cmj_mocsla.git). The housing has been printed with a radius of $R = 0.12$ m and is mounted with fifteen 2.5-in. wide-band transducers from SB Acoustics. The odd number of transducers and their low-frequency roll-off at about 100 Hz suggest adding a subwoofer, yielding a 15.1-channel layout (beamformer plus subwoofer) that proved effective in listening sessions.

Control Filter Design

This section discusses the design of control filters and its practical implementation as multiple-input, multiple-output (MIMO) finite impulse response (FIR) filter matrices.

Overview

As shown in the control overview, Figure 6, a two-band approach is proposed. The discrete transducers

only control the modal sound field up to a frequency limit, above which spatial aliasing will cause ripple in the frequency-specific beampatterns and frequency responses. At this spatial aliasing frequency, the system uses a crossover from modal beamforming to Ambisonics panning. To accomplish panning using the same Ambisonics input format as the modal beamformer, the AllRAD approach is adopted from Zotter and Frank (2012). Encoding into a sufficiently high order (e.g., fifth or seventh order) reduces the number of activated loudspeakers by means of a narrow directional mapping, and thus helps to reduce spatial aliasing in the upper frequency band.

Linkwitz-Riley Band Splitting

A Linkwitz-Riley crossover is composed of two cascaded low-pass Butterworth filters for the low band and two cascaded high-pass Butterworth filters for the high band (cf. D'Appolito 1987). The correspondingly squared Butterworth frequency high- and low-pass responses exhibit -6 dB at the crossover frequency f_c , and their phase is either strictly opposite or strictly matching at every frequency. Summing the bands with the suitable sign ensures a flat response when gains are equal, or a well-behaved interference when gains differ. We utilized cascaded third-order Butterworth filters for a sixth-order crossover between the two bands.

MIMO Crosstalk Canceler

The reduced stiffness of the air enclosed when mounting the loudspeakers in a common enclosure can support beamforming by reducing the acoustic load on the loudspeakers, in particular at low frequencies. But it also introduces acoustic crosstalk that needs to be dealt with for beamforming (Zotter et al. 2017). If one transducer is moved by a signal, the others will start to move passively, but beamforming requires independent control of the transducers.

Formally, our $L \times L$ MIMO system \mathbf{T} can be described as

$$\mathbf{v}(\omega) = \mathbf{T}(\omega) \mathbf{u}(\omega). \quad (18)$$

For brevity and to support readability, the following discussion keeps all filter formalism in the frequency domain, with the notation of the frequency dependency omitted. System inversion yields the voltage signals \mathbf{u} for a decoupled control of cone velocities.

$$\mathbf{u} = \mathbf{T}^{-1} \mathbf{v}. \quad (19)$$

A full system inversion would result in both flat magnitude responses of the direct paths and crosstalk cancellation over the whole frequency range, but it can lead to acausal filters and infeasibly long impulse responses in the time domain. Focusing on crosstalk cancellation, we reduce the effort by equalizing the MIMO system so that all its diagonal entries assume the bandpass-shaped mean transducer response H_{mean} , with the minimum-phase equalizers $H_{\text{eq},l}$,

$$\begin{aligned} T_{ll} H_{\text{eq},l} &= H_{\text{mean}}, & \text{for } l = 1, \dots, L, \\ \mathbf{h}_{\text{eq}} &= [H_{\text{eq},l}]_{l=1, \dots, L}. \end{aligned} \quad (20)$$

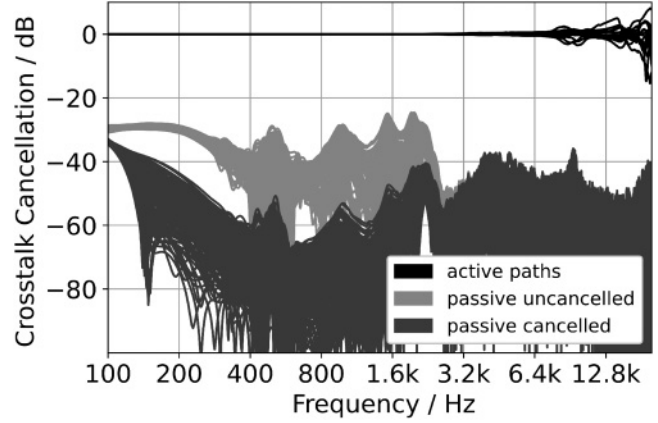
yielding the correspondingly equalized MIMO system

$$\mathbf{T}_{\text{eqd}} = \mathbf{T} \text{diag}\{\mathbf{h}_{\text{eq}}\} = H_{\text{mean}} \mathbf{I} + \mathbf{T}_{\text{eqd},\text{passive}}. \quad (21)$$

Moreover, the inversion effort is regularized by discarding crosstalk responses at frequencies above

Figure 7. Crosstalk cancellation performance for the 3|9|3-array with cutoff frequencies $f_{\text{beam1}} = 100$ Hz and $f_{\text{beam2}} = 2.9$ kHz. Loudspeaker

crosstalk is reduced to levels below -40 dB, which allows independent transducer control necessary for beamforming.



and below certain cutoff frequencies by means of a zero-phase bandpass filter on the passive off-diagonal responses

$$\tilde{\mathbf{T}}_{\text{eqd}} = H_{\text{mean}} \mathbf{I} + \mathbf{T}_{\text{eqd},\text{passive}} H_{\text{BP}}. \quad (22)$$

Altogether, inversion times the mean active response yields a matching and crosstalk-canceling system \mathbf{X}_c

$$\mathbf{X}_c = \text{diag}\{\mathbf{h}_{\text{eq}}\} \tilde{\mathbf{T}}_{\text{eqd}}^{-1} H_{\text{mean}}. \quad (23)$$

In the frequency range of the bandpass ($H_{\text{BP}} = 1$, so $\tilde{\mathbf{T}}_{\text{eqd}} = \mathbf{T}_{\text{eqd}}$) this equalization yields the crosstalk-canceled system $\mathbf{T} \mathbf{X}_c$. As a proof, the components of \mathbf{X}_c can be inserted, $\mathbf{T} \text{diag}\{\mathbf{h}_{\text{eq}}\} \tilde{\mathbf{T}}_{\text{eqd}}^{-1} H_{\text{mean}}$, to verify crosstalk cancellation and active response matching

$$\mathbf{T} \text{diag}\{\mathbf{h}_{\text{eq}}\} \text{diag}\{\mathbf{h}_{\text{eq}}\}^{-1} \mathbf{T}^{-1} H_{\text{mean}} = \mathbf{I} H_{\text{mean}} \quad (24)$$

within the bandpass range. Figure 7 shows the crosstalk-cancellation performance for the 3|9|3 array with the response H_{mean} removed. Within the bandpass range ($f_{\text{beam1}} = 125$ Hz to $f_{\text{beam2}} = 2.9$ kHz) we have little deviation among active responses (curves at 0 dB) and cancellation by up to 20 dB.

Table 3. Cutoff Frequencies for Filter Banks

	f_0	f_1	f_2	f_3	f_4
3 9 3	82	146	250	318	450
ico-04	38	77	141	209	253

Frequencies f_b in Hz.

Low-Frequency Beamforming below Aliasing

Zotter and Frank (2019, ch. 7.3.1, Equation 7.14) describe filters $B_b(\omega)$ of an equal-phase filter-bank design (D’Appolito 1987) to regularize the theoretical inverse propagator $\text{diag}\{\mathbf{h}_M(\omega)\}^{-1}$ in Equation 14 with practically limited loudspeaker excursion, and we include band-dependent order weights $w_{nm}^{(b)}$ and inverse aperture a_n^{-1} to define the radiation control

$$\mathbf{f}(\omega) = \left[i^{-n} k h'_n(kR) a_n^{-1} \sum_{b=n}^N B_b(\omega) w_{nm}^{(b)} e^{ikR} \right]_{n,m \in M}. \quad (25)$$

The weights $w_{nm}^{(b)}$ are obtained from Equation 6 but with summation in the numerator and denominator limited to the band-specific order b instead of N . Combined with the frequency-independent decoder \mathbf{Y}_M^+ (shown in Table 2), radiation control yields the target velocities

$$\mathbf{v} = \mathbf{Y}_M^+ \text{diag}\{\mathbf{f}(\omega)\} \mathbf{y}_M(\boldsymbol{\theta}_{\text{beam}}). \quad (26)$$

The cutoff frequencies of the filter bank $B_b(\omega)$ were chosen to ensure a limited loudspeaker excursion across the frequency bands, and their array-specific values are found in Table 3.

High-Frequency AllRAD Panning

In the high-frequency band, the only filtering operation should be on-axis equalization of the transducers. Beamforming is replaced by directional amplitude panning, which is accomplished by encoding the source direction $\mathbf{y}_N(\boldsymbol{\theta}_{\text{beam}})$ of sufficiently high order, e.g. $N = 5$ or higher, and AllRAD (Zotter

and Frank 2012) to approximate vector-base amplitude panning (VBAP, see Pulkki 1997) from the Ambisonically steered input signals. The spherical harmonics are first evaluated at $J = 5,100$ virtual t-design points, which can be interpreted as a decoder to many virtual transducers,

$$\mathbf{Y}_{N,J} = [\mathbf{y}_N(\boldsymbol{\theta}_1), \dots, \mathbf{y}_N(\boldsymbol{\theta}_J)]^T, \quad (27)$$

and the resulting $J = 5,100$ gains are then mapped by an $L \times J$ VBAP matrix \mathbf{G} to the L array transducers

$$\mathbf{G} = [\mathbf{g}_1, \dots, \mathbf{g}_J]. \quad (28)$$

Note that only one, two, or (in most cases) three values of \mathbf{g}_j are nonzero, depending on the direction $\boldsymbol{\theta}_j$, with $j = 1, \dots, J$. As a source beam we choose a max- \mathbf{r}_E weighted fifth-order beam and therefore need to apply order-dependent weights \mathbf{w}_N . We arrive at the precomputed $L \times (N+1)^2$ panning decoder matrix \mathbf{D}

$$\mathbf{D} = \frac{4\pi}{J} \mathbf{G} \mathbf{Y}_{N,J} \text{diag}\{\mathbf{w}_N\}. \quad (29)$$

Figure 8 shows the triangulation of the 3|9|3 layout that requires the insertion of imaginary loudspeakers, (cf. Zotter and Frank 2012). Similarly, the icosahedral layout requires imaginary loudspeakers at the array vertices to enable proper symmetric triangulation. The crossover frequency to AllRAD panning was set to $f_{c,393} = 2.9$ kHz for the 3|9|3-array ($R = 0.12$ m) and $f_{c,ico} = 1.5$ kHz for the larger IKO array ($R = 0.21$ m).

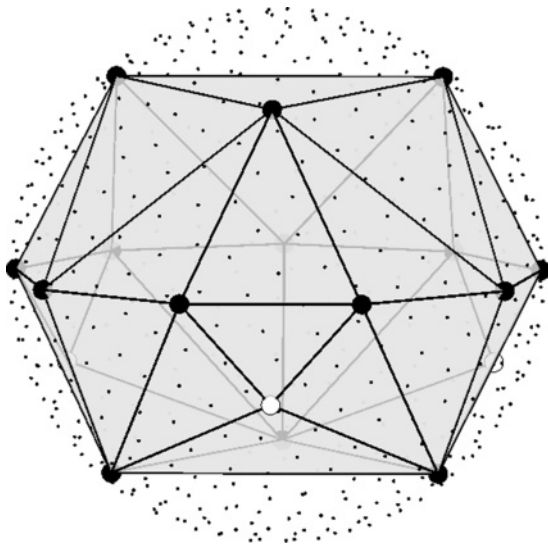
Band Summation and On-Axis Equalization

With the linear phase delay $d(\omega) = e^{-i\omega\tau}$ modeling the processing delay of the low-frequency band, we obtain the following expressions for the high- and low-frequency bands of the processing chain in Figure 6 and their final combination:

$$\begin{aligned} \mathbf{H}_1(\omega) &= H_{\text{HP}}(\omega) \mathbf{D} d(\omega), \\ \mathbf{H}_2(\omega) &= H_{\text{LP}} \mathbf{X}_c(\omega) \mathbf{Y}_M^+ \text{diag}\{\mathbf{f}(\omega)\}, \\ \mathbf{H}(\omega) &= [\mathbf{H}_1(\omega) + \mathbf{H}_2(\omega)] e(\omega). \end{aligned} \quad (30)$$

Figure 8. Triangulation of the 3|9|3-layout. Small black dots indicate the virtual AllRAD decoding layout ($J = 540$ points in this visualization). The

larger black dots mark the physical loudspeaker positions and white dots imaginary loudspeakers inserted to improve the triangulation geometry.



The last block in the processing chain is the timbral equalization $e(\omega)$ of the loudspeaker array. It flattens the frequency response of the mean of all on-axis beams (beams directed towards one of the loudspeakers), but does not influence the beam pattern. The magnitude response of the equalizer (typically a high-shelf response) is reconstructed as a minimum-phase filter and applied in the frequency domain (for a detailed description, including figures, cf. Riedel 2018, sec. 5.6).

The MIMO FIR time-domain response of $\mathbf{H}(\omega)$ is obtained by equidistant sampling in the frequency domain, using $\omega = 2\pi k/N_{\text{FFT}}$ with $k = 0, \dots, N_{\text{FFT}}/2$, and $N_{\text{FFT}} = 16,384$ points, followed by an inverse FFT to the time domain. Windowing the impulse responses to 1,024 samples is possible due to the low-latency designs, enabling real-time and live-performance applications. The real-time FIR matrix convolution can use the `jconvolver` or `mcfx_convolver` plug-ins, for instance.

Directivity Measurements

As a verification method, acoustic MIMO measurements with a surrounding semicircular microphone array were taken, similar to the measurements

taken by Schultz et al. (2018). By placing the loudspeaker array on a remotely controllable turntable, a sampling grid with a resolution of $10^\circ \times 10^\circ$ is achieved.

Horizontal and Vertical Cross Sections of Beam Patterns

Figure 9 shows the directivity patterns of horizontal beams of the 3|9|3 and IKO arrays. Both arrays are driven by the mixed-order plus high-frequency AllRAD control. The crossover to AllRAD panning reduces side-lobes for high frequencies (crossover set at $f_{c,393} = 2.9$ kHz and $f_{c,ico} = 1.5$ kHz). Due to its smaller diameter, the most effective beamforming range of the 3|9|3-array lies one octave higher than that of the IKO. Apart from this aspect, it generally achieves similar or increased directivity compared to the icosahedral array, regarding the horizontal cross section of horizontal beams. The 3|9|3 array achieves a better control of grating lobes at high frequencies, presumably due to its horizontal ring, and a similar beam focus as the icosahedral array below spatial aliasing.

Effective Orders of Directivity across Frequency

A detailed evaluation of the effectively achieved orders of directivity N_{eff} (Equation 17) regarding the different control systems and different beam directions is depicted in Figures 10, 11, and 12 (\mathbf{r}_E -measure-based analysis of the directivity). Obviously in Figure 10a, the mixed-order ico-o4 control approach effectively increases horizontal 2-D directivity by about 0.7 in the region from 400 to 800 Hz for the IKO array. Each of the two measurement-based curves stays below the predictions of the corresponding theoretical cap model (dashed lines).

The effect of the various subsystems in the control filter design is analyzed in Figure 11 for the 3|9|3 array. A frequency-independent spherical harmonics decoder \mathbf{Y}_N^+ alone hardly accomplishes beamforming of a first-order directivity below 1.6 kHz (light gray curve). Applying the limited radial filters boosts the effective beamforming order

Figure 9. Measurement-based plots of the horizontal and vertical cross-sections of horizontal beams: 3|9|3 horizontal (a), 3|9|3 vertical (b),

ico-o4 horizontal (c), and ico-o4 vertical (d). Relative dB, normalized to 0 dB for every frequency, is indicated by levels of gray (e).

Figure 10. Effective 2-D (a) and 3-D (b) orders of a horizontal beam based on directivity measurements of the IKO array showing mixed-order (ico-o4) versus third-order (ico-o3)

control filters. Dashed lines indicate model curves simulated with the spherical-cap radiation model, applying the same radial filters as in the real filter design.

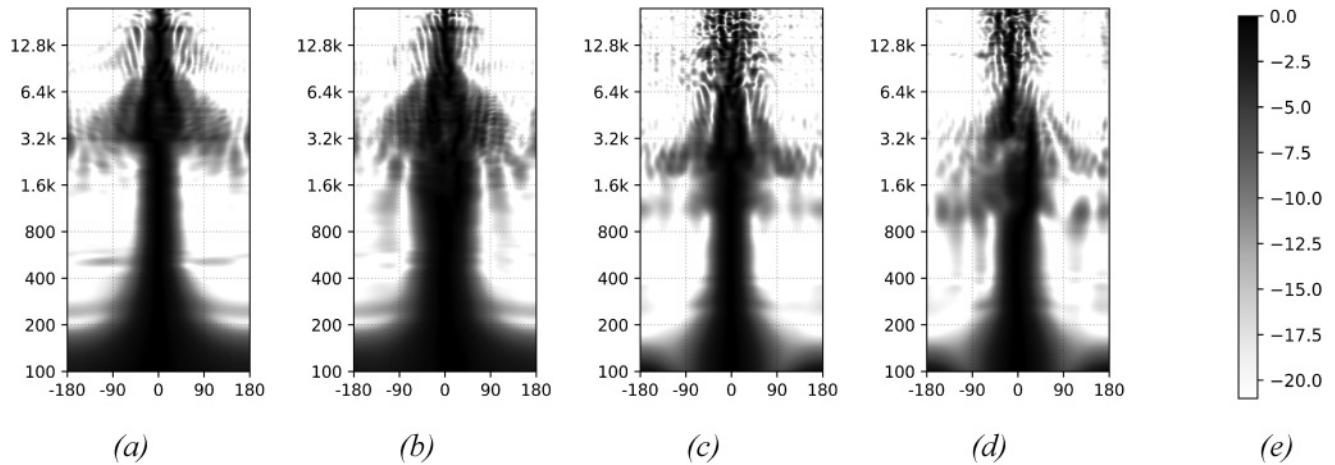


Figure 9.

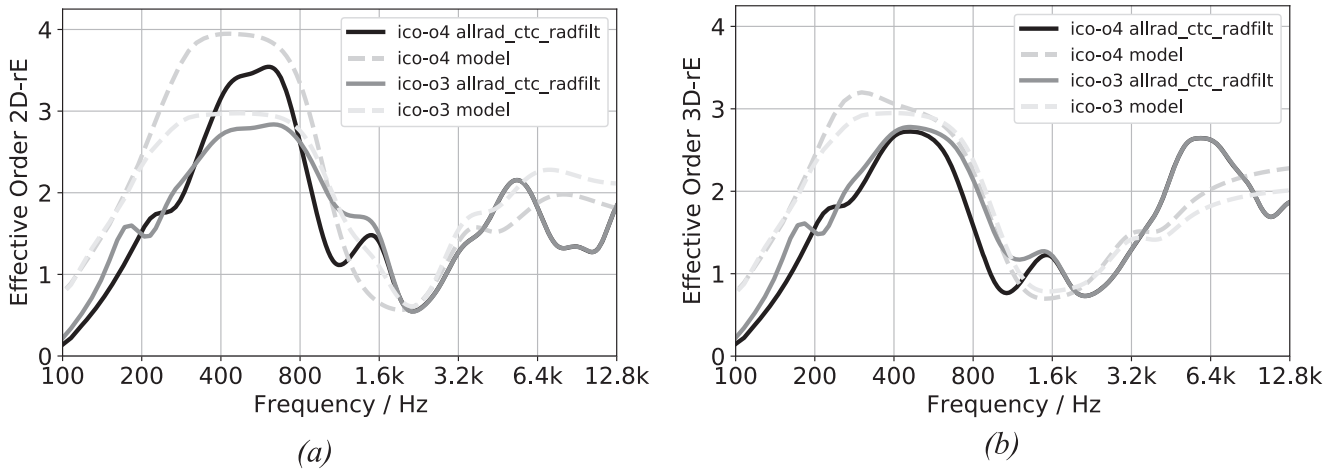


Figure 10.

(gray curve, “radfilt”) most distinctively and reaches horizontal orders of three and global 3-D orders of two. Finally, the directivity increases by up to half an order below 1.6 kHz by applying the crosstalk canceler, and above 2.9 kHz the fifth-order AllRAD Ambisonics panning provides a boost by up to one order in the 3-D map of the highest frequencies (dark curve “allrad_ctc_radfilt”). As before, the curves do not quite reach the theoretical predictions (dashed curve, “model”) in the modal beamforming range.

Figure 12 analyzes variation induced by beamforming direction. The IKO array—built with high-quality and, hence, more costly parts—maintains a similarly effective beamforming order for different beamforming directions, whereas the 3-D-printed 3|9|3 prototype varies with a peak in directivity for beams in the direction of one of its loudspeakers (20° azimuth). The measurement data is available in the Spatially Oriented Format for Acoustics, AES69-2015, and can be

Figure 11. Effective 2-D (a) and 3-D (b) orders of a horizontal beam based on directivity measurements of the 3|9|3-array showing different control-filter designs. As in Figure 10,

dashed lines indicate model curves simulated with the spherical-cap radiation model, applying the same radial filters as in the real filter design.

Figure 12. Effective 2-D orders of horizontal beams (0° to 40° azimuth) based on directivity measurements of the 3|9|3-array (a) and IKO (b),

showing the variation across the azimuth beam directions. The 3|9|3-prototype shows more variation than the IKO array.

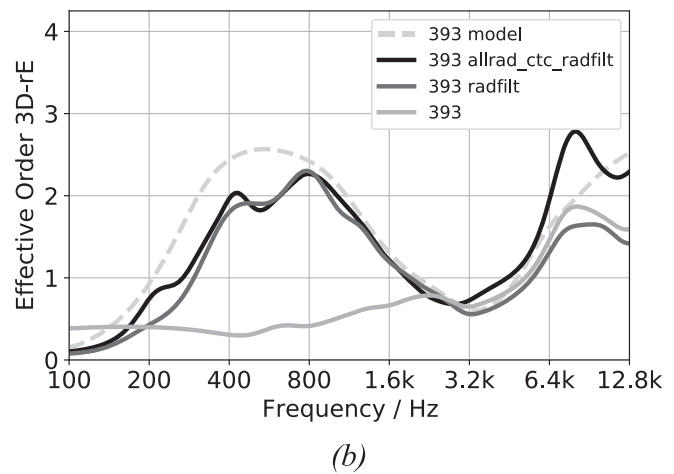
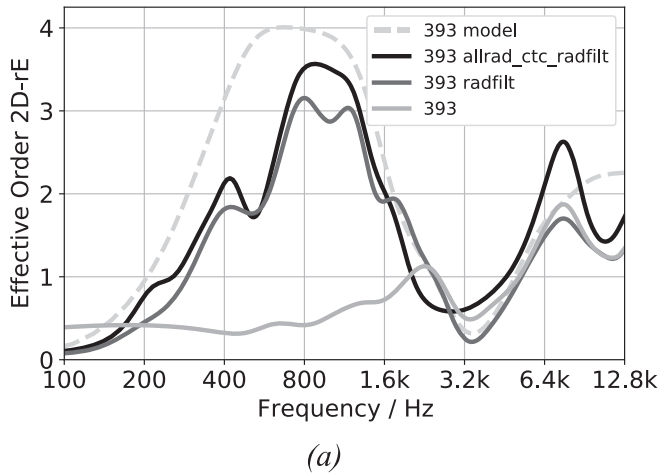


Figure 11.

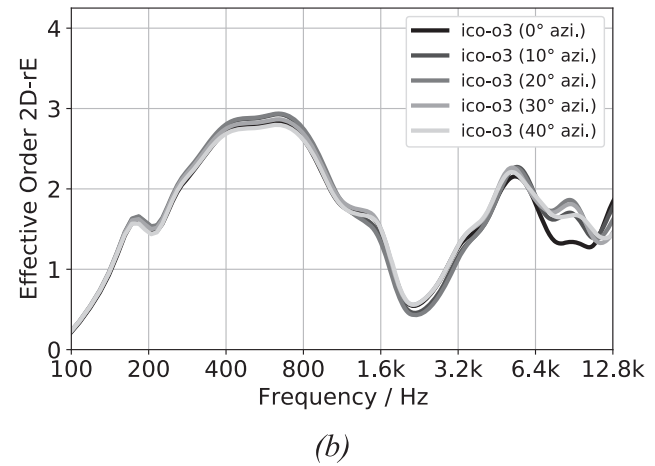
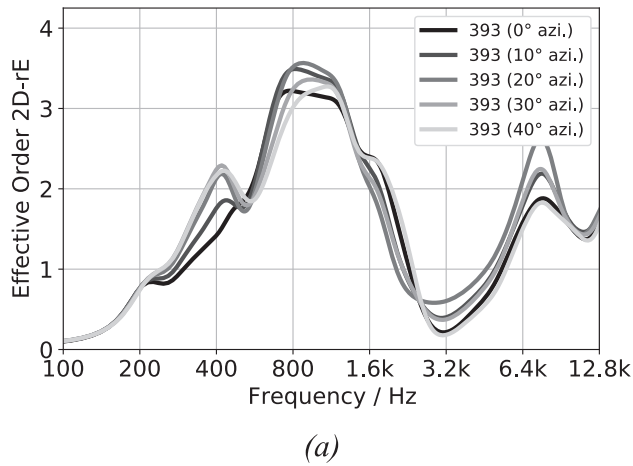


Figure 12.

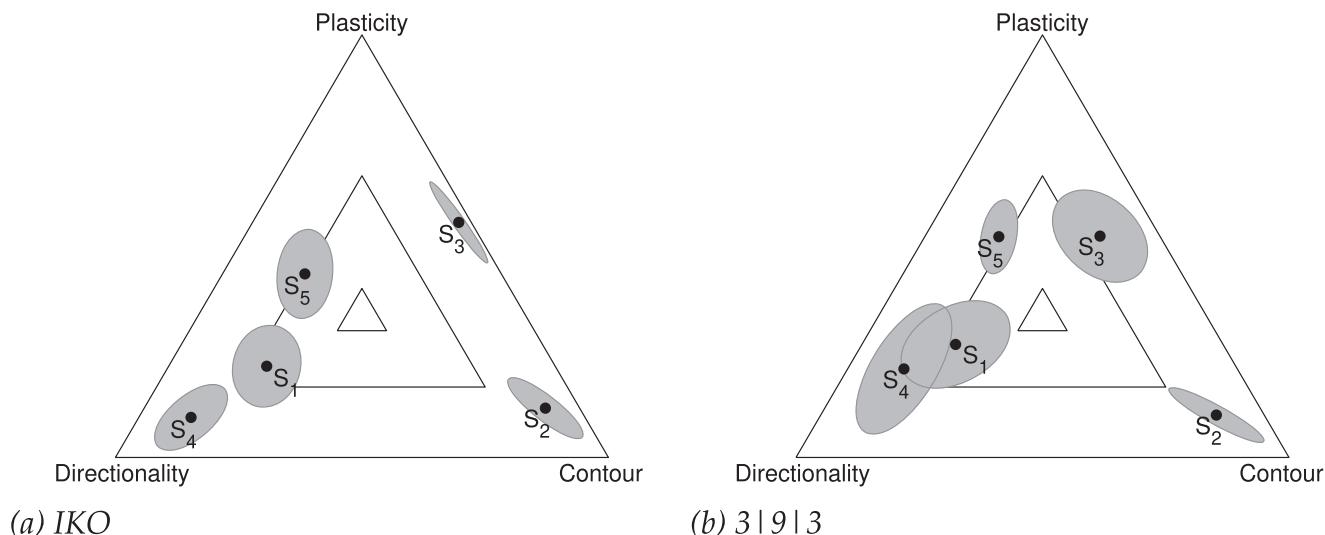
downloaded from <https://phaidra.kug.ac.at/o:91326> and <https://phaidra.kug.ac.at/o:67609>.

Listening Experiments

Above, the 3|9|3 prototype was shown to have beamforming performance similar to the more powerful and larger 20-channel IKO. Naturally,

the frequency range for beamforming is higher because of its smaller size. Although the vertical beamforming capacity is weaker compared with the IKO, the fourth-order horizontal beamforming design effectively exceeds the conventional third-order beamforming of the IKO, as used in previous tests and concerts. Because the analysis above is limited to technical beamforming measurements and metrics, this section addresses in greater detail

Figure 13. Auditory sculptural attributes of the IKO and the new 3|9|3 prototype for the musical signals composed by Sharma, Frank, and Zotter (2019). Mean values are marked by dots, the gray ellipsoidal region marks the 95% confidence ellipse (Hotelling's T-squared distribution, in gray) around each condition.



the question of whether the auditory impressions achievable with the 3|9|3 are comparable to those of the IKO. We adopt some of the perceptual analysis methods established in previous studies on the IKO to clarify the 3|9|3-prototype's potential to be used as an affordable, personal electroacoustic musical instrument.

Work by Wendt et al. (2017a) and by Laitinen et al. (2015) discusses the option of pointing beams towards or away from the listener as means of positioning auditory objects in terms of distance. Moreover, Wendt et al. (2017b) and Zotter et al. (2017) show that time-varying beamforming is capable of moving auditory objects through the interior of the playback environment. Sharma, Frank, and Zotter (2019) establish and evaluate three auditory sculptural attributes produced by a small set of signals laid out in static and time-varying beam compositions.

Listening Experiment 1: Auditory Sculpture Attributes

The listening experiment was based on comparative characterization of miniature electroacoustic compositions using a limited number of well-described sounds and their beamforming trajectories, as

defined by Sharma, Frank, and Zotter (2019, Experiment 3). The goal of the comparative rating is to evaluate the perceptual discernibility of the three sculptural qualities *directionality*, *contour*, and *plasticity*:

1. Directionality describes the potential of auditory objects in the auditory sculpture to dynamically guide the listeners attention through a room;
2. Contour describes the degree of dependency of the auditory sculpture's outline (silhouette) on the listening position, taken and imagined from temporal evolution; and
3. Plasticity describes the degree of depth grading of the spatially layered auditory objects of the auditory sculpture in the room.

The participants could switch between the looped playback of the compositions $S_1 \dots S_5$ (conditions), and for each of the conditions under comparison, the task was to find a relative position or rank within a triangular graphical interface with the corners directionality, contour, and plasticity (see Figure 13). Conditions were randomly permuted regarding the indices, playback buttons, and the movable markers shown on the interface, as in Sharma and colleagues' Experiment 3. In the present

experiment, the 3|9|3 loudspeaker was set up at the same position and in the same environment as the 2019 experiment. Twelve listeners took part, and, except for one participant, the comparison task was done twice. One comparative rating task took the participants an average time of about 4 minutes. In total, there were 21 ratings per condition.

Figure 13 compares the results obtained for the 3|9|3 prototype with the results obtained in the 2019 experiment for the IKO array (whose statistics used 29 data points per condition). The rating of the conditions in the sculptural quality space is quite similar, and the mostly contoured, unidirectional condition S_2 can be considered identical between both experiments. Condition S_4 , which used a horizontally circular beam trajectory of pink noise, was rated less directional for the 3|9|3 prototype than for the IKO. Informal reports by the listeners suggest that the contour of the auditory object is not compact and smooth in space but rather jumps and occasionally exhibits two separate high- and low-frequency auditory objects. Our hypothesis is that the increase of the directivity and higher operational beamforming frequency range of the 3|9|3 prototype might isolate the wall reflections better, but this also causes an inconsistent auditory object trajectory, with low frequencies dispersed. Moreover, the horizontal loudspeakers of the IKO aim, in alternation, at the elevations $\pm 11^\circ$ and so might never excite the wall reflections as targeted at high frequencies. A similar consideration could be used to argue that the conditions S_1 and S_5 have been rated less directional and as having a higher plasticity.

Listening Experiment 2: Auditory Object Trajectories

The second listening experiment is aligned with the test design and conditions tested by Wendt et al. (2017b) and Zotter et al. (2017) using the IKO, but here the experiment is instead tested with the 3|9|3 loudspeaker, set up at the same position and in the same environment. Six conditions were used that represented three different trajectories, each presented with two different sound stimuli

(continuous pink noise and a grain sequence). The three investigated trajectories are:

1. a beam towards the listener, fading the Ambisonics order from five to zero (omnidirectional) and back (using the size knob in the VST plugin `ambix_encoder`),
2. a circular rotation starting left and moving its horizontal beam clockwise, and
3. a cross-fade from a sound beam toward the left wall to one pointing to the right wall.

As in the prior experiments with the IKO, the experimental task used a GUI implemented with Pure Data to position ten markers that each represented the auditory event location at half a second within the looped playback time (each of the conditions was five seconds long).

There were 13 participants, and it took them on average 24 minutes to complete the task. Each participant was tested with the six stimuli in a random permutation, each test performed twice to permit checking for consistency of ratings. Data from the first, ninth, and tenth participants were discarded because their standard deviation for repeated ratings exceeded 2 m.

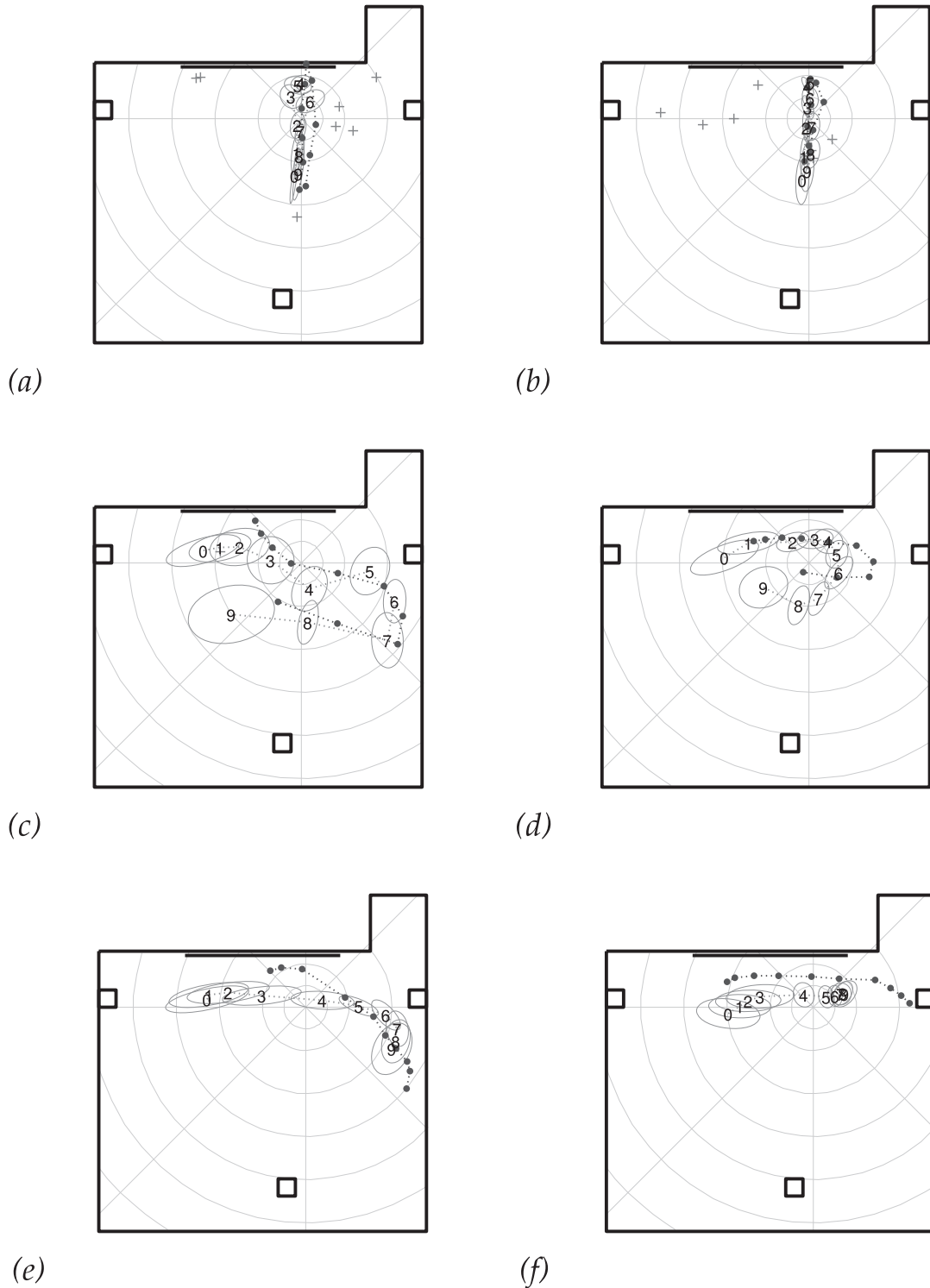
Figure 14 shows the statistical analysis of the two-dimensional results. Outliers outside the Mahalanobis distance of three standard deviations have been removed (cross symbols, only occurring in the two front-to-back tests), and the plot shows the 95% confidence regions of the mean and the mean for each the time index (13 responses were analyzed per time index). For comparison, the dark gray dots show the results taken from the IKO studies (Wendt et al. 2017b; Zotter et al. 2017).

Although auditory front-to-back trajectories of the grain signals (Figure 14b) yield a slightly larger spatial span for the 3|9|3 array (ellipses in light gray) than for the IKO (dark gray dots), we see an opposite tendency for the front-to-back movement of the noise signal in Figure 14a, in which the IKO condition spans a larger range. In any case, the monotonic mapping is qualitatively matching. The full rotation of noise in Figure 14c shows that beamforming on the 3|9|3 array appears to be superior, or at least equally capable, in projecting stationary broadband sound to lateral walls. The

Figure 14. Half-second localization ratings for three time-variant beam layouts with noise and grain signals: front-to-back noise (a), front-to-back grains (b), full-rotation noise (c), full-rotation

grains (d), left-to-right noise (e), and left-to-right grains (f). The numerals 0–9 are the time indices for the 3|9|3-array. The numeral positions mark the mean of 13 responses, and the gray filled ellipse

around each shows the 95% confidence region. The dark gray dots are the results for the IKO, taken from previous studies (Wendt et al. 2017b; Zotter et al. 2017).



3|9|3 auditory trajectories in Figures 14c and 14d cover a greater area and, although they are similar to those of the IKO, their details differ and the trajectory in the latter is offset. A comparable, if not superior, control seems to be confirmed by the dedicated left-to-right movement of noise in Figure 14e. In contrast, the transient grain stimuli in Figures 14d and 14f are not fully lateralized to the right wall as with the IKO. Perhaps as in Experiment 1, the difference in the details can be explained by the loudspeaker directions of the IKO, which imply a $\pm 11^\circ$ deflection of high-frequency content from the horizontal plane.

Despite the fact that there are noticeable differences in the precise shapes of the ratings, we assume that the results match sufficiently well for practical applications.

Conclusion

We have presented a mixed-order control theory that extends beamforming technology with compact spherical loudspeaker arrays. To evaluate the design goal of an improved horizontal beam control, we used a radiation model and introduced the effective horizontal (2-D) and global (3-D) order measures, first to prove the concept on Platonic-solid loudspeaker arrays. Mixed-order control increases the effective horizontal beamforming order from second to third order for the dodecahedral loudspeaker array, and from third to fourth order for the icosahedral array, with negligible impact on the effective 3-D order.

New mixed-order layouts were introduced that are composed of three loudspeaker rings. The dedicated mixed-order layouts save transducers while achieving equal or higher beam orders in the horizontal plane. They are especially suited for the proposed high-frequency AllRAD panning as many on-axis loudspeaker directions are aligned with the horizontal plane to support horizontal amplitude panning directions for a better directivity focus of high frequencies.

Based on directivity measurements of the IKO and the proposed 3-D-printable and inexpensive prototype of the 3|9|3 loudspeaker, we could prove the practical feasibility and effectiveness of the

proposed control-filter design based on beamforming with radial filters and crosstalk cancellation at low frequencies, and AllRAD panning at high frequencies.

Two listening experiments that were introduced and tested with the IKO loudspeaker in previous publications were repeated with the new 3|9|3 prototype. They confirm the practical applicability of the new loudspeaker as it achieves results in terms of auditory-sculpture qualities and auditory-object trajectories that are similar to those of the IKO, which is more powerful but more expensive. This makes the 3|9|3 loudspeaker an alternative, potentially a personal, electroacoustic musical instrument.

We point readers to a repository at https://git.iem.at/s1330219/cmj_mocsla.git, which contains open-source code for filter design and directivity plots as well as CAD files for 3-D-printing. We also refer the reader to the open measurement data at <https://phaidra.kug.ac.at/o:91326> and <https://phaidra.kug.ac.at/o:67609>.

Acknowledgments

We thank Gerriet K. Sharma for setting up the conditions of the listening experiments with the 3|9|3 loudspeaker, Sharma and Valerian Drack for conducting the listening experiments, the voluntary participants of these experiments, and the Austrian Knowledge Transfer Centre South (WTZ-Süd, PI at KUG/IEM: Robert Höldrich) for enabling a substantial part of our work.

This article is a revised and extended version of the paper “Design and Control of Mixed-Order Spherical Loudspeaker Arrays” (Riedel, Zotter, and Höldrich 2019), presented at the International Computer Music Conference.

References

- Avizienis, R., et al. 2006. “A Compact 120 Independent Element Spherical Loudspeaker Array with Programmable Radiation Patterns.” In *Proceedings of the 120th Convention of the Audio Engineering Society*, paper 6783.

- Chang, J., and M. Marschall. 2018. "Periphony-Lattice Mixed-Order Ambisonic Scheme for Spherical Microphone Arrays." *IEEE/ACM Transactions on Audio, Speech, and Language Processing* 26(5):924–936. 10.1109/TASLP.2018.2800290
- Daniel, J. 2001. "Représentation de champs acoustiques, application à la transmission et à la reproduction de scènes sonores complexes dans un contexte multimédia." PhD dissertation, University of Paris VI.
- D'Appolito, J. 1987. "Active Realization of Multiway All-Pass Crossover Systems." *Journal of the Audio Engineering Society* 35(4):239–245.
- Gräf, M. 2013. "Efficient Algorithms for the Computation of Optimal Quadrature Points on Riemannian Manifolds." PhD dissertation, Chemnitz University of Technology, Faculty of Mathematics.
- Laitinen, M.-V., et al. 2015. "Controlling the Perceived Distance of an Auditory Object by Manipulation of Loudspeaker Directivity." *Journal of the Acoustical Society of America* 137(6):EL462–EL468. 10.1121/1.4921678
- Marschall, M. 2014. "Capturing and Reproducing Realistic Acoustic Scenes for Hearing Research." PhD dissertation, Technical University of Denmark, Department of Electrical Engineering, Lyngby, Denmark.
- Pasqual, A. M., et al. 2010. "Application of Acoustic Radiation Modes in the Directivity Control by a Spherical Loudspeaker Array." *Acta Acustica united with Acustica* 96(1):32–42. 10.3813/AAA.918253
- Pollow, M., and G. K. Behler. 2009. "Variable Directivity for Platonic Sound Sources Based on Spherical Harmonics Optimization." *Acta Acustica united with Acustica* 95(6):1082–1092. 10.3813/AAA.918240
- Pulkki, V. 1997. "Virtual Sound Source Positioning Using Vector Base Amplitude Panning." *Journal of the Audio Engineering Society* 45(6):456–466.
- Riedel, S. 2018. "Compact Spherical Loudspeaker Arrays: New Filter and Layout Ideas." Master's thesis, University of Music and Performing Arts Graz, Institute of Electronic Music and Acoustics.
- Riedel, S., F. Zotter, and R. Höldrich. 2019. "Design and Control of Mixed-Order Spherical Loudspeaker Arrays." In *Proceedings of the International Computer Music Conference*.
- Schultz, F., M. Zaunschirm, and F. Zotter. 2018. "Directivity and Electro-Acoustic Measurements of the IKO." In *Proceedings of the 144th Convention of the Audio Engineering Society*, e-Brief 444.
- Sharma, G. K., M. Frank, and F. Zotter. 2019. "Evaluation of Three Auditory-Sculptural Qualities Created by an Icosahedral Loudspeaker." *Applied Sciences* 9(13):Art. 2698. 10.3390/app9132698
- Warusfel, O., P. Derogis, and R. Causse. 1997. "Radiation Synthesis with Digitally Controlled Loudspeakers." In *Proceedings of the 103rd Convention of the Audio Engineering Society*, paper 4577.
- Wendt, F., et al. 2017a. "Auditory Distance Control Using a Variable-Directivity Loudspeaker." *MDPI Applied Science* 7(7):Art. 666.
- Wendt, F., et al. 2017b. "Perception of Spatial Sound Phenomena Created by the Icosahedral Loudspeaker." *Computer Music Journal* 41(1):76–88. 10.1162/COMJ_a_00396
- Zotter, F., and M. Frank. 2012. "All-Round Ambisonic Panning and Decoding." *Journal of the Audio Engineering Society* 60(10):807–820.
- Zotter, F., and M. Frank. 2019. *Ambisonics: A Practical 3D Audio Theory for Recording, Studio Production, Sound Reinforcement, and Virtual Reality*. Berlin: Springer.
- Zotter, F., and R. Höldrich. 2007. "Modeling Radiation Synthesis with Spherical Loudspeaker Arrays." In *Proceedings of the International Congress on Acoustics*, pp. 508–513.
- Zotter, F., et al. 2017. "A Beamformer to Play with Wall Reflections: The Icosahedral Loudspeaker." *Computer Music Journal* 41(3):50–68. 10.1162/comj_a_00429